Kinetic regulation of kinesin's two motor domains coordinates its stepping along microtubules

Yamato Niitani[1]‡, Kohei Matsuzaki[1,2]‡, Erik Jonsson[3], Ronald D. Vale[3] & Michio Tomishige[1,2]*

[1]Department of Applied Physics, School of Engineering, The University of Tokyo, Tokyo 113-8656, Japan, [2]Department of Physical Sciences, College of Science and Engineering, Aoyama Gakuin University, Sagamihara 252-5258, Japan, [3]Howard Hughes Medical Institute and Department of Cellular and Molecular Pharmacology, University of California, San Francisco, CA 94158, United States

‡ *These authors contributed equally to this work.*

*Correspondence should be addressed to: tomishige@phys.aoyama.ac.jp

ABSTRACT

The two identical motor domains (heads) of dimeric kinesin-1 move in a hand-over-hand along a microtubule, coordinating their ATPase cycles such that each ATP hydrolysis is tightly coupled to a step and the motor can take many steps without dissociating. The neck linker, a structural element that connects the two heads, has been shown to be essential for the head-head coordination; however, which kinetic step(s) in the chemomechanical cycle is "gated" by the neck linker remains unresolved. Here, we employed pre-steady state kinetics and single molecule assays to investigate how the neck linker conformation affects kinesin's motility cycle. We show that the neck linker conformation in the front kinesin head confers higher affinity for microtubules, but does not change ATP affinity. In contrast, the neck linker conformation in the rear kinesin head increases ATP affinity by several thousand-fold compared to the front head but has little effect on microtubule affinity. These conformation-specific effects in combination favor ATP hydrolysis and dissociation of rear head prior to microtubule detachment of the front head, thereby providing a kinetic explanation for the coordinated walking mechanism of dimeric kinesin.

INTRODUCTION

Kinesin-1 (hereafter called kinesin) is a dimeric motor protein that moves along microtubule to carry cellar cargos inside most eukaryotic cells. The unidirectional motion of kinesin is driven by an N-terminal globular domain (termed "head") that catalyzes ATP hydrolysis and binds to the microtubule. The head is followed by a 14 amino-acid segment called the "neck linker" and then a long coiled-coil stalk that dimerizes the two identical polypeptide chains. Single dimeric kinesin moves processively along microtubules in a hand-over-hand manner by alternately moving the two heads in an 8-nm step toward the plus-end of the microtubule (Vale and Milligan, 2000; Asenjo et al., 2003; Kaseda et al., 2003; Asbury et al., 2003; Yildiz et al., 2004; Isojima et al., 2016; Wolff et al., 2023). The cycle of binding and dissociation of the head to/from microtubule is tightly correlated with the ATPase cycle; ADP release stabilizes the microtubule binding of the head, while phosphate release after ATP hydrolysis induces detachment of the head from the microtubule (Gilbert and Johnson, 1994; Ma and Taylor, 1997a; Cross, 2004). Therefore, to alternately move the two heads, the ATP hydrolysis cycles in the rear and/or front heads should be differentially regulated ("gated"), such that the rear head hydrolyzes ATP and detaches from microtubule, prior to the front head (Hackney 1994; Ma and Taylor, 1997b; Gilbert et al., 1998; Auerbach and Johnson, 2005a; Cochran 2015).

To gate the ATPase cycles during processive movement, there must be a structural mechanism that enables the two heads to communicate with one another. When both heads are bound to the adjacent tubulin-binding sites ("two-head-bound state"), the front and rear heads are separated by 8 nm and cannot directly interact with each other. However, their neck linkers are highly extended and adopt two distinct configurations; the neck linker in the front head is stretched backward and the neck linker in the rear head is pointing forward, favoring the docked state (**Figure 1A;** Rice et al., 1999; Skiniotis et al., 2003; Tomishige et al., 2006; Liu et al., 2017). Artificially extending the neck linkers by inserting polypeptide spacers reduces the coupling ratio between forward step and ATP turnover, indicating that the strain transmitted through the neck linkers has an essential role for the

head-head coordination (Hackney et al., 2003; Yildiz et al., 2008; Shastry and Hancock, 2010; Andreasson et al., 2015; Isojima et al., 2016).

Several models, which are not mutually exclusive, have been put forth to explain the alternating catalysis of the two heads and high coupling between ATP turnover and stepping (Block, 2007; Valentine and Gilbert, 2007; Gennerich and Vale, 2009). One type of model proposes neck linker-based regulation of microtubule affinity. A “rear-head gating” version of this model proposes that forward strain posed through neck linker accelerates the detachment of the rear head. Evidence supporting this model is based on experiments showing that the two-headed kinesin hydrolyzes ATP and detaches from microtubule much faster than a one-headed kinesin (Hancock and Howard, 1999; Crevel et al., 2004; Schief et al., 2004), and that the detachment rate of the head from microtubule is faster under a forward than a rearward pulling force from an optical trap (Uemura et al., 2002). However, other experimental results showed that the detachment rate from microtubule of the rear head of a dimer or of the monomer under assisting load was not significantly accelerated (Rosenfeld et al., 2003; Dogan et al., 2015). Another model proposes that the backward strain posed to the neck linker suppresses the detachment of the front head until the rear head detaches from microtubule; however, experimental evidence supporting this idea is lacking.

Another class of gating models proposes that a chemical transition in the ATPase cycle is sensitive to neck linker tension between the two heads. A “front-head gating” model has been proposed that tension in the two-head bound state decreases ATP binding in the front head (Rosenfeld et al., 2003; Klumpp et al., 2004; Guydosh and Block, 2006; Dogan et al., 2015). Pre-steady state kinetic measurements showed that binding of mant-ATP (a fluorescent analogue that shows a signal change upon kinesin binding) to a microtubule-docked kinesin dimer showed single exponential kinetics with a signal amplitude nearly half than that expected if both heads can bind ATP (Rosenfeld et al., 2003; Klumpp et al., 2004). However, interpreting these results is complex, since the amplitude and duration of

the mant-ATP signal is a composite from the front and rear heads, which complicates the assignment of specific rate constants of nucleotide binding and unbinding or isomerization events to the two microtubule-bound heads.

In this study, we measured the ATP-binding and microtubule-detachment kinetics (**Figure 1B**) of the front and rear heads separately using pre-steady state and single-molecule measurements. To isolate and measure the kinetics of the front and rear head states separately, we utilized two methods: 1) disulfide-crosslinking to immobilize the neck linker in monomeric kinesin in the forward- or backward- pointing configurations (mimicking the rear and front head states, respectively), and 2) a heterodimeric kinesin in which one polypeptide chain was locked in neck linker -docked, rear head conformation. Our results provide quantitative evidence that both kinesin heads participate in a coordinated gating mechanism: the backward constraint of the neck linker in the front head reduces its detachment rate from microtubules without changing ATP affinity, while the forward constraint on the neck linker in the rear head dramatically increases nucleotide affinity but has minimal effect on microtubule affinity. These results are consistent with the closed and open conformations of the nucleotide-binding pocket in the rear and front heads of microtubule-bound kinesin dimers observed in cryo-electron microscopy (cryo-EM) studies (Liu et al., 2017; Benoit et al., 2021) and provide a mechanism for the coordinated hand-over-hand movement of kinesin.

RESULTS

Controlling the neck-linker orientation of monomer kinesin through crosslinking

We first sought to examine the kinetics of nucleotide and microtubule binding to monomeric kinesin in which the neck linker was oriented either in the forward (mimicking the rear head) or the rearward (mimicking the front head) direction (**Figure 1A, C**). To control the orientation of the neck linker in monomer kinesin, we employed disulfide-crosslink between two cysteines, one on the head and the other on the neck linker (Tomishige and Vale, 2000). To immobilize the neck linker in this forward-pointing, docked conformation (Gigant et al.,

126 2013), K222 (located at the plus-end oriented tip of the head) and E334 (the distal end of the
127 docked neck linker) residues were substituted with cysteines in a Cys-light monomeric
128 kinesin (K339 Cys-light), whose solvent-exposed cysteines were replaced by either Ser or
129 Ala (Rice et al., 1999) (**Figure 1C**, left). We refer to the C222/C334 crosslink here as "rear
130 head crosslink". We previously introduced this cysteine pair into dimeric kinesin and found
131 that oxidative crosslinking resulted in a complete loss of directionality (Tomishige and Vale,
132 2000). The neck linker of the front head is detached from the head, and its distal end is pulled
133 backward (Skiniotis et al., 2003; Tomishige et al., 2006; Benoit et al., 2021). To constrain the
134 neck linker in this backward-pointing configuration, which we refer to as the "front head
135 crosslink", A47 (the minus-end-oriented base of the head) and T328 (five residues from the
136 proximal end of the neck linker) residues were substituted with cysteines (**Figure 1C**, right).
137 The cysteine pairs were covalently crosslinked by oxidative treatment with copper ion and
138 o-phenanthroline (Kobashi, 1968; Kaan et al., 2011). The crosslinking efficiencies were
139 estimated, by running SDS-PAGE under non-reducing conditions, to be 97% and 87% for
140 the rear and front head crosslinks, respectively (**Figure 1D** and **Figure 1−figure supplement**
141 **1**).
142
143 We first evaluated the effect of disulfide crosslinking on the microtubule-activated ATP
144 turnover rates (**Figure 1−figure supplement 2**). Under reducing conditions, the k_{cat} for both
145 the rear and front head crosslinks (27.0 and 32.2 ATP/s per head, respectively) were lower
146 than WT (57.1 ATP/s per head) (**Figure 1E**), which is likely caused by the mutations of the
147 residues. For the rear head crosslink, the reduced ATPase activity might also be due to the
148 presence of crosslinked species even under the reducing condition (~30%; **Figure 1D and**
149 **Figure 1−figure supplement 1B**). Under oxidized conditions, the k_{cat} values for both rear
150 and front head crosslinks were reduced by more than 10-fold compared to that under reducing
151 condition (2.2 and 1.5 ATP/s per head, respectively (**Figure 1E** and **Table 1**)).
152
153 **Effect of neck linker crosslinking on the binding/dissociation rates of ATP**

154 To measure ATP binding rate to kinesin head on the microtubule, we rapidly mixed the
155 nucleotide-free kinesin-microtubule complex with increasing concentrations of mant-ATP
156 using stopped flow apparatus. The initial rapid increase in the fluorescence represents mant-
157 ATP binding to the nucleotide pocket of the motor domain; this rapidly increasing phase was
158 fit with an exponential to obtain the observed rate k_{obs} (**Figure 2−figure supplement 1**). At
159 low mant-ATP concentrations, the k_{obs} increased linearly as a function of mant-ATP
160 concentration (Ma and Taylor, 1997a; Moyer et al., 1998); the slope of the fitted line provides
161 binding rate k_{+1} and the offset provides dissociation rate k_{-1} (**Figure 2A**). Rear head
162 crosslinking resulted in a modest decrease in the on-rate k_{+1} by three-fold (5.1 and 1.6 $s^{-1}\mu M^{-}$
163 ^{1} under reducing and oxidizing conditions, respectively; **Figure 2B**). However, rear head
164 crosslinking produced a 30-fold decrease in the off-rate k_{-1} (117 and 3.7 s^{-1} under reducing
165 and oxidizing conditions, respectively). In contrast, front head crosslinking resulted in only
166 a modest and similar 2-fold decrease in both k_{+1} and k_{-1} (k_{+1} was 4.0 and 2.0 $s^{-1}\mu M^{-1}$, k_{-1} was
167 96 and 42 s^{-1} under reducing and oxidizing conditions, respectively; **Figure 2B**), resulting in
168 little or no change in the affinity for ATP after crosslinking. These results indicate that the
169 rear head crosslink reduces the ATP dissociation rate, while the front head crosslink does not
170 significantly alter the ATP binding kinetics. We note that the measured k_{-1} of rear head
171 crosslink was similar to the ATP turnover rate k_{cat} (**Table 1**); therefore, it is likely that the
172 majority of ATP molecules bound to the head were hydrolyzed, and the observed fluorescence
173 decrease rather represents mant-ADP release.
174
175 To detect the ATP dissociation event of the rear head, one must kinetically trap the head in a
176 neck-linker docked, pre-ATP hydrolysis state such that ATP hydrolysis becomes significantly
177 slower than the ATP dissociation. To this end, we employed a mutant kinesin with a point
178 mutation of E236A in the switch II loop, which almost abolishes ATPase hydrolysis and traps
179 in the microtubule-bound, neck-linker docked state (Rice et al., 1999; Auerbach and Johnson,
180 2005b). Previous study showed that mant-ATP binding rate to dimeric kinesin was not
181 significantly affected by this mutation (Auerbach and Johnson, 2005b).
182

183 To determine the ATP off-rate k_{-1} of E236A monomer, we employed single-molecule
184 fluorescence resonance energy transfer (smFRET) between the donor dye attached to the
185 head and the acceptor dye conjugated to ATP. The residue S55, separated by ~0.8 nm from
186 the nucleotide pocket, was substituted with cysteine and was labeled with ATTO488 or Cy3
187 dye; we would expect ~90% high FRET efficiency when Alexa 647-conjugated ATP (termed
188 as Alexa-ATP) binds to the labeled head (**Figure 2−figure supplement 3A**). Using wild-type
189 kinesin dimer, we demonstrated that Alexa-ATP acts as a substrate to drive kinesin motility
190 along microtubule, although velocities were about 10-fold lower than those driven by
191 unmodified ATP (**Figure 2−figure supplement 2**). First, we observed single-molecule FRET
192 of ATTO488-labeled "wild-type" monomer on microtubule in the presence of 500 nM Alexa-
193 ATP. We observed FRET efficiency increases upon Alexa-ATP binding to microtubule-bound
194 monomer, and then the donor and acceptor simultaneously disappeared (representing that the
195 head dissociated from microtubule after ATP hydrolysis; **Figure 2C**, left), or the donor
196 fluorescence recovered after disappearance of the acceptor fluorescence (representing that
197 ATP dissociated while the head remains bound to the microtubule; **Figure 2C**, right). We
198 found that the ATP bound to wild-type head could be either hydrolyzed, followed by head
199 dissociation from the microtubule, or reversibly dissociated with nearly equal probability
200 (**Figure 2C**). This finding is consistent with the mant-ATP kinetics measurements of the
201 monomer without neck-linker constraint showing similar k_2 and k_{-1} (**Table 1**). In contrast, the
202 single-molecule FRET observation of Cy3-labeled E236A monomer in the presence of 200
203 nM Alexa-ATP showed that the majority of the Cy3-labeled mutant remained bound to the
204 microtubule during the observation period, and Alexa-ATP molecules repeatedly bound and
205 reversibly dissociated to/from the mutant head (**Figure 2D**). The mean dwell time of the high
206 FRET state (ATP-bound state) was 1.54 s, which corresponds to k_{-1} of 0.65 s^{-1} (**Figure 2E**
207 and **Figure 2−figure supplement 3B**); 140-fold smaller than that of the wild-type monomer
208 (91 s^{-1}). We note that the neck linker of the E236A monomer was neither pulled forward nor
209 constrained by crosslinking; therefore, the ATP off-rate of monomeric E236A may still be
210 faster than that of the rear head in dimeric kinesin (as will be examined later).
211

212 **Effect of neck linker crosslinking on the dissociation rate from microtubule**

213 Next, we analyzed the effect of the neck-linker crosslinking on the detachment rate of the
214 monomeric kinesin from microtubule (MT dissociation). First, we measured turbidity change
215 after rapidly mixing the nucleotide-free kinesin-microtubule complex with 1 mM ATP using
216 stopped-flow apparatus. Since monomeric kinesin repeatedly hydrolyzes ATP per encounter
217 to the microtubule through electrostatic interactions (Jiang and Hackney, 1997), we included
218 150 mM KCl to prevent reassociation of the detached head. However, the rear head crosslink
219 kinesin did not show any initial burst in turbidity after oxidative treatment (**Figure 3–figure**
220 **supplement 1**), because it was weakly bound, even in the absence of ATP, and dissociated in
221 the presence of 150 mM KCl. In contrast, the front head crosslink kinesin displayed an initial
222 burst phase for MT dissociation under these salt conditions. The fit of the initial decay
223 revealed a 7-fold decrease in the MT dissociation rate k_2 (51.5 and 7.0 s^{-1} for reduced and
224 oxidized conditions, respectively (**Figure 3A**)).

225

226 Since we could not measure the MT dissociation for the rear head using light scattering, we
227 sought an alternate approach involving visualizing GFP-fused K339 Cys-light kinesin
228 binding to/from the microtubule using single-molecule fluorescent microscopy in the
229 presence of 100 mM KCl and 1 mM ATP (**Figure 3B**). The rear head crosslink showed a 6-
230 fold reduced binding frequency to microtubule (**Figure 3–figure supplement 2A**). We fit
231 the histograms of the dwell time of fluorescent spots on microtubule with single exponential
232 decay (**Figure 3–figure supplement 2B**) and employed the inverse of the dwell time as a
233 rough estimate of the dissociation rate (termed as k_{2_SMF}). The k_{2_SMF} of the rear head
234 crosslink was slightly increased compared to before crosslinking (47.2 and 57.1 s^{-1} under
235 reducing and oxidizing conditions, respectively). In contrast, the front head crosslink showed
236 an 18-fold decrease in the k_{2_SMF} compared to before crosslinking (42.1 and 2.3 s^{-1} under
237 reducing and oxidizing conditions, respectively) (**Figure 3C** and **Table 1**). These results
238 suggest that forward constraint on the neck linker in the rear head does not significantly
239 accelerate the detachment from microtubule, while backward constraint of the neck linker in
240 the front head reduces the detachment rate.

241

242 **Different crosslinking schemes to examine the role of the neck-linker docking on gating**
243 The reduced detachment rate of the front head crosslink is likely due to the inability of the
244 C47/C328 crosslinked head to adopt the neck-linker docked conformation. Then, we asked
245 whether the reduced detachment rate can be recovered if the crosslinked neck linker is
246 allowed to partially dock onto the head. To test this, we crosslinked the neck linker in the
247 backward orientation between C47 on the head and C335 on the neck linker (**Figure 3D**,
248 right), which produces an extra 7 amino acids compared to C47/C328 between the base and
249 the crosslinked residues on the neck linker, allowing the initial few residues of the neck linker
250 (including I325 residue involved in filling the hydrophobic pocket exposed on the ATP-bound
251 head (Vale and Milligan, 2000; Sindelar, 2011; Cao et al., 2014)) to dock onto the head
252 (**Figure 3–figure supplement 3**). The ATP-induced detachment rate k_2 of C47/C335 showed
253 only two-fold reduction after crosslinking (41.6 and 19.4 s^{-1} for reduced and oxidized
254 conditions, respectively, measured using light scattering; **Figure 3A, C** and **Figure 3–figure**
255 **supplement 4C-E**). This finding is consistent with the idea that the gatekeeper of the front
256 head gate is the neck-linker docking and suggests that partial neck linker docking onto the
257 head is sufficient to half open the gate, although more extensive neck linker docking would
258 be required to fully open the gate.
259

260 In contrast, the neck linker orientation in the rear head crosslink did not change the
261 dissociation rate from microtubules but reduced the dissociation rate of ATP (**Figure 2B**). We
262 examined an alternate crosslinking scheme between C4 on the N-terminal stretch and C330
263 on the neck linker (Tomishige and Vale, 2000), which couples the neck linker (NL) with the
264 N-terminal flexible segment called "cover strand (CS)" (**Figure 3D**, left). The interaction
265 between the neck linker and cover strand has been shown to be important to produce a
266 forward-bias in the diffusional motion of the detached head against hindering load (Hwang
267 et al., 2008; Khalil et al., 2008). The ATP dissociation rate k_{-1} was not significantly affected
268 by C4/C330 crosslinking (148^{-1} and 96 s^{-1} for reduced and oxidized conditions, respectively;
269 **Figure 3E** and **Figure 3–figure supplement 4B**), indicating that the interaction of the neck

linker with the head, not with the N-terminal cover strand, is responsible for the reduction of the ATP off-rate.

A E236A-WT heterodimer to distinguish front and rear heads

The front head crosslink was designed to constrain the neck linker to mimic the neck linker orientation of the front head. However, it differs from that of the front head in that the backward-pointing configuration is maintained by the crosslinking, not by the backward strain originating from the stretched neck linkers between two microtubule-bound heads (Hyeon and Onuchic, 2007; Hariharan and Hancock, 2009). We sought to further investigate how the neck linker tension contributes to the front head gating by examining the microtubule detachment kinetics of the front head in the context of a dimeric kinesin. To this end, we employed a heterodimer in which one polypeptide is wild-type (WT) and the other contains the E236A mutation (E236A-WT heterodimer). As described above, E236A mutant acts as a long-lived rear head, which is kinetically trapped in the neck-linker docked, pre-ATP hydrolysis state. Thus, in the E236A-WT heterodimer in the presence of ATP, one would expect the E236A head to be in the rear and the WT head to occupy the front.

To test this assumption, we used the smFRET sensor, which has been used to distinguish the configurations of two heads (Mori et al., 2007). We first introduced one cysteine into the residue 215 (located at the plus-end oriented tip of the head) of the E236A chain and another into the residue 43 (located at the minus-end oriented base of the head) of WT chain and labeled with Cy3 and Cy5 fluorophores (**Figure 4–figure supplement 1**, left). The FRET efficiency of dual-labeled molecules bound to the microtubule in the presence of ATP showed a single peak at about 90%. When we introduced 43Cys into the E236A chain and 215Cys into the WT chain, however, the distribution of the FRET efficiency showed a single peak at about 10% (**Figure 4–figure supplement 1**, right). These results are consistent with E236A-WT heterodimer stably taking two-head-bound state, in which WT head is in the front and E236A head is in the rear position.

First, we measured the steady-state microtubule-activated ATPase activity of the E236A-WT heterodimer. The microtubule-activated ATPase k_{cat} of the E236A-WT heterodimer was 4.6 ATP/s per head (**Figure 6–figure supplement 1**), suggesting that the front WT head is capable of hydrolyzing ATP, but its catalytic activity is suppressed (c.f. ~30 ATP/s per head for wild-type dimer (Tomishige and Vale, 2000)).

Detachment rate of the front head of E236A-WT heterodimer

Then, we measured ATP-induced detachment rate k_2 of the front WT head of E236A-WT heterodimer from microtubule using high-speed single-molecule microscopy (**Figure 4A**; Isojima et al., 2016). We labeled WT head with gold nanoparticle (40 nm in diameter) and observed the motion of the gold probe attached to E236A-WT heterodimer on the microtubule in the presence of 1 mM ATP. With the temporal resolution of the measurement (50 μs), we could clearly identify transient increases in the fluctuation of the gold probe accompanied by detachment of the labeled head (**Figure 4B** and **Figure 4–figure supplement 2**). The direction of the displacement of the gold probe upon unbinding was opposite to kinesin's forward step, which was very rarely observed for E236A-WT heterodimer (**Figure 4–figure supplement 3**). These observations demonstrate that the labeled WT head was in the leading position, as expected, prior to detachment. The mean dwell time of the bound and unbound states of the front head at 1 mM ATP was 160 and 11 ms, respectively (**Figure 4C** and **Figure 4–figure supplement 4**).

To determine the rate constants for the ATP-promoted detachment rate of the front WT head, we measured the dwell time of microtubule-bound state of the gold-labeled WT head under various ATP conditions (**Figure 4D** and **Figure 4–figure supplement 4**). The mean dwell time increased as ATP concentration was decreased (**Figure 4E**), indicating that the bound dwell time includes ATP-binding and hydrolysis in the front head. The inverse of the mean dwell time plotted against ATP concentration could be well fit with a Michaelis-Menten equation with fit parameters of k_{cat} = 6.3 ± 0.2 s^{-1} and K_m = 43 ± 6 μM (**Figure 6D**). The observed k_{cat} also includes ADP release rate; however, since ADP release (~5 ms) becomes

328 negligible within the dwell time of >160 ms, we took this k_{cat} as an approximation of the
329 ATP-promoted detachment rate k_2. The k_2 determined using E236A-WT heterodimer (6.3 s^{-1}
330) is similar to the k_2 of front head crosslink (7.0 s^{-1}), supporting the notion that the backward
331 strain posed to the neck linker significantly reduces ATP-induced detachment rate of the front
332 head.
333
334 **ATP dissociation rate of the rear E236A head of the heterodimer**
335 Next, we measured the ATP-dissociation rate k_{-1} of the E236A rear head of the heterodimer
336 on microtubule and compared it with the rate of monomeric E236A (**Figure 2E**), to
337 investigate how forward strain applied to the neck linker affects ATP dissociation kinetics.
338 We used smFRET to measure the ATP off-rate, with a donor Cy3 on the E236A rear head
339 (after cysteine modification of S43 residue) and an acceptor Alexa-ATP; we expected ~80%
340 high FRET when Alexa-ATP bound to the rear E236A head (the distance between dyes is
341 ~2.5 nm), and low FRET when ATP bound to the front wild-type head (the dye distance ~9
342 nm) (**Figure 5A**). The mean dwell time of the high FRET state was 65.5 s, which corresponds
343 to k_{-1} of 0.015 s^{-1} (**Figure 5B, C**). This ATP off-rate is 42-fold smaller than that of the E236A
344 monomer (**Figure 5D**), indicating that forward strain further increases the affinity of the
345 E236A head for ATP.
346
347 **Effect of the neck-linker tension on the gating of the front and rear heads**
348 Experimental results obtained from neck-linker crosslinking monomers and the E236A-WT
349 heterodimer revealed that distinct chemical steps are gated in the front and rear heads (k_2 and
350 k_{-1} respectively). We next sought to examine whether neck linker tension places a role in
351 gating these steps. To reduce the tension posed to the neck linker in the two-head-bound state,
352 we extended the neck linker of E236A-WT heterodimer by inserting 7 or 12 poly-Gly
353 between neck linker and neck coiled-coil of both chains (referred to as G7 and G12) (**Figure**
354 **6A**; Isojima et al., 2016). The microtubule-activated ATPase rate of G12 increased modestly
355 by 1.6-fold compared to that of the heterodimer without neck-linker extension (referred to as
356 G0) (**Figure 6B and Figure 6–figure supplement 1**).

We first examined the effect of the tension posed to the neck linker on ATP-induced detachment rate k_2 of the front head, by observing the neck-linker extended E236A-WT heterodimer using high-speed dark-field microscopy. The gold probe attached to the front WT head of G7 and G12 heterodimers showed transient increases in the fluctuation of the gold probe (**Figure 6C**). The inverse of the dwell time of bound state for G7 and G12 mutants (**Figure 6–figure supplement 2, 3**) plotted against ATP concentration fit well with the Michaelis-Menten equation (**Figure 6D**); the fit parameters are k_{cat} = 7.6 ± 0.9 s^{-1} and K_m = 22 ± 10 μM for G7 and k_{cat} = 9.3 ± 0.7 s^{-1} and K_m = 6.1 ± 2.1 μM for G12. The k_2 modestly increased as the inserted poly-Gly number increased; G12 showed 1.5-fold increase in k_2 compared to G0 (**Figure 6E**), reminiscent of the results of ATPase rates (**Figure 6B**). The detached WT head of G12 heterodimer occasionally bound to the rear-tubulin binding site (the frequency was 14% among all binding events), however, the head detached from the rear-binding position much faster (19 ms at 1 mM ATP; **Figure 6–figure supplement 4**) than from the front-binding site (111 ms), indicating that the orientation of the neck linker has greater effect on the front head gating than the tension. These findings demonstrate that the detachment rate of the front head is not greatly affected by the amount of tension posed to the neck linker, at least within the range of 12 poly-Gly insertions.

Next, we examined the effect of the tension posed to the neck linker on ATP off-rate k_{-1} of the rear E236A head of the E236A-WT heterodimer, by measuring smFRET between Cy3-labeled E236A head and Alexa-ATP. When compared to the heterodimer without neck linker extension (0.015 s^{-1}; **Figure 5C**), k_{-1} determined from the inverse of the mean dwell time of the high FRET state only modestly increased for G7 (0.018 s^{-1}) and increased by 5-fold for G12 (0.081 s^{-1}) (**Figure 5D** and **Figure 5–figure supplement 1**). The k_{-1} was further increased for monomeric E236A without neck linker constraint as described before (0.65 s^{-1}; **Figure 2E and 5D**). These results indicate that the ATP off-rate of the rear E236A head is significantly affected by the amount of the forward strain, especially when the neck linker was extended with more than 7 poly-Gly insertions.

386

387 **DISCUSSION**

388 To identify the chemical transition that is gated in the front and/or rear head, we measured
389 ATP binding and microtubule detachment kinetics of kinesin's catalytic domain with neck
390 linker constraints 1) imposed by disulfide crosslinking of the neck linker in monomeric
391 kinesin in backward (rear head -like) and forward (front head -like) orientations, and 2) using
392 the E236A-WT heterodimer to create a two-head microtubule-bound state with the mutant
393 and WT heads occupying the rear and front positions respectively. The results from these two
394 experimental approaches and using different measurements approaches yielded consistent
395 results. In the front head, backward orientation of the neck linker has little effect on ATP
396 binding and dissociation rates. These findings differ from a prevailing view that the ATP-
397 binding step is gated in the front head (Rosenfeld et al., 2003; Klumpp et al., 2004; Guydosh
398 and Block, 2006; Dogan et al., 2015). However, we find that the ATP-induced detachment
399 rate of the front head from *microtubule* (k_2) is reduced by the backward-oriented position of
400 the neck linker, suggesting that a step subsequent to ATP binding (either an isomerization
401 event that occurs after ATP binding, ATP hydrolysis or Pi release) is gated in the front head.

402

403 We also provide evidence for a rear-head gating mechanism that involves a tighter affinity
404 for ATP (due to a decrease in reversible ATP-dissociation rate k_{-1}) without a change in
405 microtubule affinity in the ATP-bound state. The dissociation constant K_d of ATP for the rear
406 E236A head of the E236A-WT heterodimer is estimated to be about 10 nM, assuming that
407 the ATP on-rate is similar to that of the rear head crosslink (Auerbach and Johnson, 2005b).
408 In contrast, the K_d of ATP for the front head crosslink and the monomer without constraint
409 were similar (~20 μM), which is about 2,000-fold greater than that of the rear head. A
410 difference in the ATP-affinity between the front and rear heads can explain previous
411 experimental results supporting the front-head gating mechanism (Uemura and Ishiwata,
412 2003; Rosenfeld et al., 2003; Klumpp et al., 2004; Guydosh and Block, 2006; Dogan et al.,
413 2015), although our direct kinetic measurements show that this difference is manifest through
414 in a stronger affinity for ATP in the rear head rather than a weaker affinity in the front head.

415 While the neck linker position of the rear head increases the affinity of bound ATP, it does
416 not significantly accelerate k_2, which includes the ATP hydrolysis and Pi release steps in the
417 chemical cycle.
418
419 **Kinetic gating aids head-head coordination but does not prevent progression through**
420 **the ATPase cycle**
421 Our results show that the front head gate slows down but not does not block its ATPase cycle.
422 The ATP-induced microtubule detachment rate k_2 of the front head is 6-7 s^{-1} (7.0 s^{-1} for the
423 front head monomer crosslink and 6.3 s^{-1} for the front head of E236A-WT heterodimer)
424 which is similar to its overall ATPase rate (4.6 s^{-1}). These rate constants are sufficiently low
425 to keep the catalytic cycles of two heads largely out of phase, since the detachment rate of
426 the rear head of wild-type dimer (inverse of the dwell time from two-head-bound state to
427 one-head-bound state during processive movement) is ~100 s^{-1} (Isojima et al., 2016). The
428 observed detachment of the front head of E236A-WT heterodimer is likely caused by ATP
429 hydrolysis of the front head, because 1) ATP turnover rate of this heterodimer was similar to
430 the k_2 value, and 2) the dwell time of the bound state of the front head on microtubule was
431 dependent on the ATP concentration. These results suggest that the kinesin's head can slowly
432 hydrolyze ATP and detach from microtubule without the aid of neck-linker docking. This
433 idea can explain how kinesin dimer takes repetitive back steps under large hindering loads.
434 Carter and Cross (2005) showed that kinesin takes 8-nm backward steps at supra-stall forces
435 (>7 pN) exerted using an optical trap, and that the stepping rate was dependent on the ATP
436 concentration (~0.3 steps/s and ~1 step/s at 1 mM and 10 μM ATP conditions, respectively),
437 which are comparable to the dwell times that we found for the microtubule-bound state of
438 the front head of E236A-WT heterodimer (0.16 s and 1.1 s at 1 mM and 10 μM ATP,
439 respectively; **Figure 4–figure supplement 4**). These results suggest that the back steps are
440 likely caused by the neck-linker docking-independent slow ATP catalysis of the front head
441 followed by its dissociation from the microtubule in ADP-bound state.
442
443 **A kinetic and structural model for kinesin gating**

The ~2,000-fold difference in the ATP binding affinity between the front (low affinity) and rear (high affinity) heads suggests a structural difference in their nucleotide binding pockets. Indeed, the high ATP affinity state of the neck linker -docked rear head is consistent with a "closed" nucleotide pocket observed in crystal and cryo-EM structures of kinesin-1 bound to tubulin and complexed with a non-hydrolyzable ATP analog in kinesin's active site (Shang et al., 2005; Gigant et al., 2013). Moreover, a recent high-resolution cryo-EM image of the microtubule-bound KIF14 dimer showed that while they could observe nucleotide in the active site of the front head, the structure of the pocket was more "open" and rather similar to that of a nucleotide-free head (Shang et al., 2014; Cao et al., 2014; Benoit et al., 2021). Since the switch I and II loops that are involved in hydrolysis reaction are away from the γ-phosphate in the opened nucleotide pocket, the open state is incompatible with ATP hydrolysis, while the closed state is competent in ATP hydrolysis (Kull and Endow, 2002; Parke et al., 2010) (**Figure 7–figure supplement 1B**). Thus, these structural features are consistent with our kinetics results.

These findings suggest that the isomerization from the open to closed conformational state, rather than the chemical transition, is gated by the neck linker constraint (**Figure 7–figure supplement 2**). This aligns with our structural modeling of kinesin dimer in the two-head-bound state (Makino et al., 2024), which showed that conformational transitions are suppressed for both the front head (from open to closed state) and the rear head (from closed to open state), as these changes would cause an intolerable increase in tension on the disordered neck linker region (**Figure 7**). We demonstrated that neck linker docking is responsible for opening the gate (i.e., the open to closed transition) using the loose backward crosslink of the neck linker (**Figure 3A-D**). The C47/C335 crosslink forms a short 7-amino acid flexible loop, which is insufficient for the formation of two β-sheets (residues 326-334) (**Figure 3–figure supplement 3**). However, it allows the conformational transition of the initial segment of the neck linker (residues 323-325); K323 and T324 residues form an α-helix extending the C-terminus of α6, while the I325 residue docks onto the hydrophobic pocket exposed on the closed head. Given that the hydrophobic pocket is positioned forward

473 from the neck linker's base (**Figure 7–figure supplement 1A**), the docking of the I325 side
474 chain is suppresses in the front head, as it would cause an intolerable increase in tension
475 (entropy decrease) on the disordered neck linker (Makino et al., 2024), maintaining the open
476 state. The neck linker extension had a smaller effect on front-head gating (**Figure 6E**), likely
477 because a stable interaction between the I325 side chain and the hydrophobic pocket is
478 necessary to maintain the closed state until ATP hydrolysis completes. In contrast, the neck
479 linker extension had a larger effect on the rear head's ATP affinity (**Figure 5D**). This is
480 probably because the rear head can occasionally transition back to an open state (followed
481 by reversible ATP release) without tension on the neck linker (**Figure 2C**; Rice et al., 2003).
482 Thus, forward strain plays a crucial role in aiding I325 residue docking and stabilizing the
483 closed state.
484
485 In summary, our findings, together with structural data discussed above, are consistent with
486 an asynchronous sequence of events in the front and rear kinesin heads that help to coordinate
487 their chemomechanical cycles to ensure their continuous stepping along the microtubule
488 (**Figure 7**). In the rear head, ATP binding is followed rapidly by an isomerization step that
489 closes the nucleotide pocket, decreasing the rate of nucleotide dissociation and facilitates
490 ATP hydrolysis. This conformational change is facilitated by docking of the neck linker in its
491 forward orientation (Benoit et al., 2003). In the front head, in contrast, the backward
492 conformation of neck linker favors an open nucleotide pocket, which helps to prevent the
493 microtubule-bound front head from proceeding with ATP hydrolysis before the rear head
494 detaches. Once the rear head detaches, the front head "gate" is relieved, allowing the neck
495 linker to dock and its nucleotide pocket to close. This asynchrony in the timing of ATP
496 hydrolysis minimizes the likelihood of both heads simultaneously entering an ADP-state and
497 dissociating from microtubule. Recent cryo-EM studies and modeling of the kinesin dimer
498 under various nucleotide states support the proposal that the open-closed conformational
499 transition is gated by the neck linker strain; however, direct evidence for this conformational
500 transition in the context of a processively moving kinesin dimer would help to further
501 substantiate this model.

Acknowledgments

We thank M. Nakajima and Y. Sakai for support with cloning. M.T. was supported by MEXT KAKENHI Grant Number 17H03661 and by JSPS KAKENHI Grant Numbers JP20H05542, JP22H04850.

Author contributions

Yamato Niitani, Conceptualization, Investigation, Formal analysis, Software, Methodology, Visualization; Kohei Matsuzaki, Investigation, Formal analysis, Software, Methodology, Visualization; Erik Jonsson, Investigation, Methodology; Ronald Vale, Methodology, Supervision, Funding acquisition, Writing – review and editing; Michio Tomishige, Conceptualization, Methodology, Supervision, Funding acquisition, Writing – original draft, Project administration, Writing - review and editing

516 **REFERENCES**

517 Aitken, C. E., Marshall, R. A. & Puglisi, J. D. An oxygen scavenging system for
518 improvement of dye stability in single-molecule fluorescence experiments. *Biophys. J.*
519 **94**, 1826–1835 (2008).
520 Andreasson, J. O. L. *et al.* Examining kinesin processivity within a general gating
521 framework. *eLife* 2015;4:e07403.
522 Asbury, C. L., Fehr, A. N. & Block, S. M. Kinesin moves by an asymmetric hand-over-
523 hand mechanism. *Science* **302**, 2130-2134 (2003).
524 Asenjo, A. B., Krohn, N. & Sosa, H. Configuration of the two kinesin motor domains
525 during ATP hydrolysis. *Nature Struct. Biol.* **10**, 836-842 (2003).
526 Auerbach, S. D. & Johnson, K. A. Alternating site ATPase pathway of rat conventional
527 kinesin. *J. Biol. Chem.* **280**, 37048-37060 (2005a).
528 Auerbach, S. D. & Johnson, K. A. Kinetic effects of kinesin switch I and switch II mutants.
529 *J. Biol. Chem.* **280**, 37061-37068 (2005b).
530 Benoit M. P. M. H. *et al*. Structural basis of mechano-chemical coupling by the mitotic
531 kinesin KIF14. *Nat. Commun.* **12**, 3637 (2021).
532 Benoit, M. P. M. H., Hunter, B., Allingham, J. S. & Sosa, H. New insights into the
533 mechanochemical coupling mechanism of kinesin-microtubule complexes from their
534 high-resolution structures. *Biochem. Soc. Trans.* **51**, 1505-1520 (2023).
535 Block, S. M. Kinesin motor mechanics: binding, stepping, tracking, gating, and limping.
536 *Biophys. J.* **92**, 2986-2995 (2007).
537 Cao, L. *et al*. The structure of apo-kinesin bound to tubulin links the nucleotide cycle to
538 movement. *Nat. Commun.* **5**, 5364 (2014).
539 Carter, N. J. & Cross, R. A. Mechanics of the kinesin step. *Nature* **435**, 308-312 (2005).
540 Cochran, J. C. Kinesin motor enzymology: chemistry, structure, and physics of nanoscale
541 molecular machines. *Biophys. Rev.* **7**, 269-299 (2015).
542 Crevel, I. M.-T. *et al*. What kinesin does at roadblocks: the coordination mechanism for
543 molecular walking. *EMBO J.* **23**, 23-32 (2004).
544 Cross, R. A. The kinetic mechanism of kinesin. *Trends Biochem. Sci.* **29**, 301-309 (2004).

545 Denoncin, K., Nicolaes, V., Cho, S.-H., Leverrier, P. & Collet, J.-F. Protein disulfide bond
546 formation in the periplasm: determination of the in vivo redox state of cysteine residues.
547 *Methods Mol. Biol.* **966**, 325-336 (2013).
548 Dogan, M. Y., Can, S., Cleart, F. B., Purde, V. & Yildiz, A. Kinesin's front head is gated by
549 the backward orientation of its neck linker. *Cell Rep.* **10**, 1967-1973 (2015).
550 Gennerich, A. & Vale, R. D. Walking the walk: how kinesin and dynein coordinate their
551 steps. *Curr. Opin. Cell Biol.* **21**, 59-67 (2009).
552 Gigant, B. *et al*. Structure of a kinesin–tubulin complex and implications for kinesin
553 motility. *Nat. Struct. Mol. Biol*. **20**, 1001–1007 (2013).
554 Gilbert, S. P. & Johnson, K. A. Pre-steady-state kinetics of the microtubule-kinesin
555 ATPase. *Biochemistry* **33**, 1951-1960 (1994).
556 Gilbert, S. P., Moyer, M. L. & Johnson, K. A. Alternating site mechanism of the kinesin
557 ATPase. *Biochemistry* **37**, 792-799 (1998).
558 Guydosh, N. R. & Block, S. M. Backsteps induced by nucleotide analogs suggest the front
559 head of kinesin is gated by strain. *Proc. Natl. Acad. Sci. USA* **103**, 8054-8059 (2006).
560 Hackney, D. D. Evidence for alternating head catalysis by kinesin during microtubule-
561 stimulated ATP hydrolysis. *Proc. Natl. Acad. Sci. USA* **91**, 6865-6869 (1994).
562 Hackney, D. D., Stock, M. F., Moore, J. & Patterson, R. A. Modulation of kinesin half-site
563 ADP release and kinetic processivity by a spacer between the head groups. *Biochemistry*
564 **42**, 12011-12018 (2003).
565 Hancock, W. O. & Howard, J. Kinesin's processivity results from mechanical and chemical
566 coordination between the ATP hydrolysis cycles of the two motor domains. *Proc. Natl.*
567 *Acad. Sci. USA* **96**, 13147-13152 (1999).
568 Hariharan, V. & Hancock, W. O. Insights into the mechanical properties of the kinesin neck
569 linker domain from sequence analysis and molecular dynamics dimulations. *Cel Mol*
570 *Bioeng* **2**, 177–189 (2009).
571 Hwang, W., Lang, M. J. & Karplus, M. Force generation in kinesin hinges on cover-neck
572 bundle formation. *Structure* **16**, 62-71 (2008).

573 Hyeon, C. & Onuchic, J. N. Internal strain regulates the nucleotide binding site of the
574 kinesin leading head. *Proc. Natl. Acad. Sci. USA* **104**, 2175-2180 (2007).
575 Isojima, H., Iino, R., Niitani, Y., Noji, H. & Tomishige, M. Direct observation of
576 intermediate states during the stepping motion of kinesin-1. *Nature Chem. Biol*. **12**, 290-
577 297 (2016).
578 Jiang, W. & Hackney, D. D. Monomeric kinesin head domains hydrolyze multiple ATP
579 molecules before release from a microtubule. *J. Biol. Chem.* **272**, 5616–5621 (1997).
580 Kaan, H. Y. K., Hackney, D. D. & Kozielski, F. The structure of the kinesin-1 motor-tail
581 complex reveals the mechanism of autoinhibition. *Science* **333**, 883-885 (2011).
582 Kaseda, K., Higuchi, H. & Hirose, K. Alternate fast and slow stepping of a heterodimeric
583 kinesin molecule. *Nature Cell Biol.* **5**, 1079-1082 (2003).
584 Klumpp, L. M., Hoenger, A. & Gilbert, S. P. Kinesin's second step. *Proc. Natl. Acad. Sci.*
585 *USA* **101**, 3444-3449 (2004).
586 Khalil, A. S. *et al.* Kinesin's cover-neck bundle folds forward to generate force. *Proc. Natl.*
587 *Acad. Sci. USA* **105**, 19247-19252 (2008).
588 Kobashi, K. Catalytic oxidation of sulfhydryl groups by *o*-phenanthroline copper complex.
589 *Biochim. Biophys. Acta* **158**, 239-245 (1968).
590 Kull, F. J. & Endow, S. A. Kinesin: switch I & II and the motor mechanism. *J. Cell Sci.*
591 **115**, 15-23 (2002).
592 Liu, D., Liu, X., Shang, Z. & Sindelar, C. V. Structural basis of cooperativity in kinesin
593 revealed by 3D reconstruction of a two-head-bound state on microtubule. *eLife*
594 2017;6:e24490.
595 Ma, Y.-Z. & Taylor, E. W. Kinetic mechanism of a monomeric kinesin construct. *J. Biol.*
596 *Chem.* **272**, 717-723 (1997a).
597 Ma, Y.-Z. & Taylor, E. W. Interacting head mechanism of microtubule-kinesin ATPase. *J.*
598 *Biol. Chem.* **272**, 724-730 (1997b).
599 Makino, T. *et al.* Tension-induced suppression of allosteric conformational changes
600 explains coordinated stepping of kinesin-1. bioRxiv ?? (2024).

601 Mori, T., Vale, R. D. & Tomishige, M. How kinesin waits between steps. *Nature* **450**, 750-
602 754 (2007).
603 Moyer, M. L., Gilbert, S. P. & Johnson, K. A. Pathway of ATP hydrolysis by monomeric
604 and dimeric kinesin. *Biochemistry* **37**, 800–813 (1998).
605 Parke, C. L., Wojcik, E. J., Kim, S. & Worthylake, D. K. ATP hydrolysis in Eg5 kinesin
606 involves a catalytic two-water mechanism. *J. Biol. Chem.* **285**, 5859-5867 (2010).
607 Rice, S. *et al*. A structural change in the kinesin motor protein that drives motility. *Nature*
608 **402**, 778-784 (1999).
609 Rice S. *et al.* Thermodynamic properties of the kinesin neck-region docking to the catalytic
610 core. *Biophys. J.* **84**, 1844-1854 (2003).
611 Rosenfeld, S. S. *et al*. Stepping and stretching: how kinesin uses internal strain to walk
612 processivity. *J. Biol. Chem.* **278**, 18550-18556 (2003).
613 Schief, W. R., Clark, R. H., Crevenna, A. H. & Howard, J. Inhibition of kinesin motility by
614 ADP and phosphate supports a hand-over-hand mechanism. *Proc. Natl. Acad. Sci. USA*
615 **101**, 1183-1188 (2004).
616 Shang, Z. *et al.* High-resolution structures of kinesin on microtubules provide a basis for
617 nucleotide-gated force-generation. *eLife* 2014;3:e04686.
618 Shastry, S. & Hancock, W. O. Neck linker length determines the degree of processivity in
619 kinesin-1 and kinesin-2 motors. *Curr. Biol.* **20**, 939-943 (2010).
620 Sindelar, C. V. A seesaw model for intermolecular gating in the kinesin motor protein.
621 *Biophys. Rev.* **3**, 85-100 (2011).
622 Skiniotis, G. *et al*. Nucleotide-induced conformations in the neck region of dimeric kinesin.
623 *EMBO J.* **22**, 1518-1528 (2003).
624 Tomishige, M. & Vale, R. D. Controlling kinesin by reversible disulfide cross-linking:
625 identifying the motility-producing conformational change. *J. Cell Biol.* **151**, 1081-1092
626 (2000).
627 Tomishige, M., Stuurman, N. & Vale, R. D. Single-molecule observations of neck linker
628 conformational changes in the kinesin motor protein. *Nature Struct. Mol. Biol.* **13**, 887-
629 894 (2006).

630 Uemura, S. *et al.* Kinesin-microtubule binding depends on both nucleotide state and
631 loading direction. *Proc. Natl. Acad. Sci. USA* **99**, 5977-5981 (2002).
632 Uemura, S. & Ishiwata, S. Loading direction regulates the affinity of ADP for kinesin.
633 *Nature Struct. Biol.* **10**, 308-311 (2003).
634 Vale, R. D. & Milligan R. A. The way things move: looking under the hood of molecular
635 motor proteins. *Science* **288**, 88-95 (2000).
636 Valentine, M. T. & Gilbert, S. P. To step or not to step? How biochemistry and mechanics
637 influence processivity in kinesin and Eg5. *Curr. Opin. Cell Biol.* **19**, 75-81 (2007).
638 Wolff, J. O. *et al*. MINFLUX dissects the unimpeded walking of kinesin-1. *Science* **379**,
639 1004-1010 (2023).
640 Yildiz, A., Tomishige, M., Vale, R. D. & Selvin, P. R. Kinesin walks hand-over-hand.
641 *Science* **303**, 676-678 (2004).
642 Yildiz, A., Tomishige, M., Gennerich, A. & Vale, R. D. Intramolecular strain coordinates
643 kinesin stepping behavior along microtubules. *Cell* **134**, 1030-1041 (2008).
644
645

646 ## Materials and methods

647 **DNA cloning and protein purification**

648 We used a 339 amino-acid "cysteine-light" mutant or a 349 amino-acid wild-type human
649 kinesin-1 monomer as a template for mutagenesis. Cysteines and/or a E236A point-
650 mutation were introduced by PCR cloning involving QuikChange mutagenesis (Stratagene)
651 (Tomishige and Vale, 2000). For heterodimer, mutations were introduced into one of the
652 two polypeptide chains of the cysteine-light kinesin-1 heterodimer with 490 amino-acids
653 (Tomishige et al., 2006; Isojima et al., 2016). For single molecule fluorescent observation
654 of monomers, GFP (P64L/S65T variant) was fused at the C-terminal of constructs. All the
655 constructs were verified by DNA sequencing. Kinesin proteins were expressed and purified
656 as described previously (Tomishige and Vale, 2000; Tomishige et al., 2006) except that for
657 monomeric kinesins, Ni-NTA chromatography was followed by dialysis against 25 mM
658 PIPES (pH 7.0), 100 mM NaCl, 2 mM $MgCl_2$ and 100 μM ATP for 3 h at 4°C. EGTA in
659 the buffer was removed. For steady state ATPase assays and single molecule observations,
660 proteins were further purified with microtubule-affinity purification (Tomishige et al.,
661 2006). DTT and EGTA were removed from the solutions. Tubulin was purified and
662 polymerized as described previously (Woehlke et al., 1997). Protein concentrations were
663 determined by Bradford assays using BSA as a standard.
664

665 **Chemical cross-linking**

666 Disulfide cross-link was formed by oxidation using copper and phenanthroline (Kobashi,
667 1968; Kaan et al., 2011). Reactions were carried out by addition of 10 μM $CuCl_2$ and 20
668 μM o-phenanthroline to 4 μM kinesin heads in 25 mM PIPES (pH 6.8) plus 2 mM $MgCl_2$
669 and incubation on ice for 3 h. The reactions were quenched by addition of 1 mM EGTA.
670 Control reactions were carried out in parallel by adding 10 mM DTT. Disulfide cross-
671 linking was verified using non-reducing SDS-PAGE with AMS (4'-acetamido-4'-
672 maleimidylstilbene-2,2'-disulfonic acid, 6508; Setareh Biotech) which react with reduced
673 cysteine residues causing band-shift on SDS-PAGE (Denoncin et al., 2013). Post cross-
674 linking reaction of kinesin (after addition of EGTA) was denatured by addition of 10%

675 trichloroacetic acid (TCA) and incubation for 30 min at 4°C. 100 µl of denatured kinesin
676 solution was centrifuged (100k rpm, for 5 min) and pellet was carefully washed with 50
677 mM Tris-HCl (pH 7.5) plus 10 mM EDTA to remove DTT or copper. The pellet was then
678 resuspended in 30 µl of solution containing 50 mM Tris-HCl (pH 7.5), 10 mM EDTA,
679 0.1% SDS, 20 mM AMS. The sample was incubated over night at room temperature under
680 shaking. Addition of SDS sample buffer without reducing reagents was followed by SDS-
681 PAGE (8.5% polyacrylamide) and CBB staining. Ratio of reduced and oxidized molecules
682 was quantified using ImageJ.
683
684 **Steady state ATPase assay**
685 Microtubule-stimulated ATPase activity was measured using spectrometer (V550; JACSO)
686 with a coupled enzymatic assay as described previously (Woehlke et al., 1997). The
687 ATPase assays were performed in BRB12 buffer (12 mM PIPES (pH 6.8), 2 mM $MgCl_2$, 1
688 mM EGTA) containing 1 mM ATP, 20 µM taxol, 0.1 mg/ml casein and coupled NADH
689 oxidation system (0.2 mM NADH, 5 mM phospho(enol)pyruvate, 10 µg/ml of pyrvate
690 kinase, and 10 µg/ml of lactate dehydrogenase). 1 mM DTT was also added when
691 measuring reducing conditions. The assays were started with 10 nM kinesin and varying
692 concentrations of microtubules at 22°C.
693
694 **Pre-steady state kinetics measurements**
695 All stopped flow experiments were performed at 25°C in BRB25 buffer (25 mM PIPES
696 (pH 6.8), 2 mM $MgCl_2$, 1 mM EGTA) using a KinTek Stopped flow system (SF2004;
697 Kintek Corp., State College, PA) with a Xenon lamp. Mant-nucleotide fluorescence
698 measurements were performed using an extension wavelength of 280 nm and fluorescence
699 emission was monitored using a 445/40 band pass filter (D445/40M; Chroma Tec). 5-10
700 fluorescent traces were averaged for each experimental condition. Turbidity measurements
701 were performed at 340 nm and 15-20 turbidity traces were averaged. Averaged stopped
702 flow traces were fit to single exponential function,
703 $$y = A\, exp(-k_{obs}t) + C \qquad \text{(Eq. 1)}$$

704 or a burst equation,

705 $$y = A\,exp(-k_{obs}t) + k_{ss}t + C \qquad \text{(Eq. 2)}$$

706 where k_{obs} is the rate constant of the initial exponential phase, k_{ss} is the rate constant of the
707 linear phase, A is the amplitude of exponential phase and C is the constant term.
708

709 **Mant-ATP binding kinetics**

710 Microtubule-kinesin complex was prepared by incubation of 3.2 μM post cross-linking
711 kinesin with 4 μM microtubule and 20 μM taxol in BRB25 buffer at room temperature for
712 10 min. Microtubule-C222/C334 kinesin complex was prepared by following procedure.
713 3.2 μM of reduced/oxidized C222/C334 kinesin was incubated with 4 μM microtubules, 20
714 μM taxol and 5 U/ml apyrase at room temperature for 1 h, followed by a centrifugation
715 (80k rpm, 10 min) on 20% sucrose cushion. The pellet was resuspended in initial volume of
716 BRB25 plus 20 μM taxol. The microtubule-kinesin complex was then rapidly mixed with
717 increasing concentrations of mantATP. Fluorescence data of mantATP binding were fit to
718 single exponential (Eq. 1). Values of k_{obs} were plotted against nucleotide concentration and
719 fit to linear function,

720 $$k_{obs} = k_{+1}[\text{mantATP}] + k_{-1} \qquad \text{(Eq. 3)}$$

721 where k_{+1} is the second-order rate constant for nucleotide binding and k_{-1} is the rate
722 constant for nucleotide dissociation from the motor.
723

724 **Microtubule dissociation kinetics**

725 Microtubule-kinesin complex was prepared by incubation of 3.2 μM post cross-linking
726 kinesin with 4 μM microtubule, 20 μM taxol and 0.1 U/ml apyrase in BRB25 buffer at
727 room temperature for 10 min. 150 mM KCl was then added into kinesin solution. The
728 change in turbidity was monitored after rapid mixing of microtubule-kinesin complex with
729 ATP (1 mM post mixing) plus 150 mM KCl. Turbidity traces were fit to burst equation
730 (Eq. 2) to determine microtubule dissociation rate.
731

732 **Single molecule fluorescence observation of GFP-labeled kinesin**

733 Binding/detachment of individual GFP-fused kinesin on axonemes (purified from sea
734 urchin sperm flagella) were observed in a custom-build prism-type laser-illuminated total-
735 internal-reflection microscope as described (Tomishige and Vale, 2000). Assay chamber
736 constructed between a quartz slide and a coverslip was first filled with axonemes diluted in
737 BRB12 for 3min, followed by a washing with 1mg/ml casein in BRB12 for 3 min. The
738 chamber was then filled with the assay solution contained GFP-kinesin (200 pM for WT,
739 C47/C328 and C47/C335, 500 pM for C222/C334 and C4/C330), 1 mM ATP, 100 mM
740 KCl and oxygen scavenging system (4.5 mg/ml glucose, 50 U/ml catalase, 50 U/ml
741 glucose-oxidase) and sealed. 70 mM 2-mercaptoethanol was added in the assay solution
742 when observing in reducing condition. GFP molecules were exited at 488 nm and
743 fluorescence was recorded at 10 ms temporal resolution. Distributions of dwell time on
744 axonemes were obtained from kymographs. Fluorescent spots dwelled more than two
745 frames were used for analysis. Detachment rates were determined by single exponential
746 fitting of the dwell histograms.
747
748 **Flow-cell chamber preparation for single molecule FRET**
749 For the wild-type monomeric kinesin, flow-cell chamber was constructed between poly-L-
750 lysine-coated quartz slide and cover slip. The chamber was first filled with microtubule in
751 BRB12 buffer containing 20 μM taxol for 5 min. Then, BRB12 buffer containing 20 μM
752 taxol and 1 mg/ml casein was infused and incubated for 2 min followed by washing with
753 BRB12 buffer containing 20 μM taxol. The chamber was finally filled with observation
754 buffer containing an ATP regenerating system (10 μg/ml creatin kinase, 2 mM creatin
755 phosphate), an oxygen scavenging system (2.5 mM protocatechuic acid (PCA), 1 unit/ml
756 protocatechuate-3,4-dioxygenase (PCD) (P8279-25UN; Sigma), 2 mM Trolox) (Aitken et al.,
757 2008), 150 mM KCl, 20 μM taxol, 500 nM Alexa Fluor 647 ATP (A22362; Invitrogen) and
758 100 pM kinesin in BRB12 buffer. All procedures were carried out at room temperature.
759
760 For the other constructs (E236A monomer, E236A-WT heterodimer), flow-cell chamber was
761 constructed between quartz slide pre-cleaned with 0.1 M KOH and cover slip, separated by

762 ~50 μm thickness. The cell was first filled with Protein A (Sigma P6031-1MG) solution (20
763 μl, 50 μg/ml) in BRB12 buffer (12 mM PIPES (pH 6.8), 2 mM $MgCl_2$, 1 mM EGTA) for 2
764 min. After washing unbound protein with 40 μl of BRB12 buffer, 20 μl of 20 μg/ml anti-α-
765 tubulin antibody (Sigma T6199) solution in BRB12 buffer was infused for 5 min. Then
766 unbound antibody was washed out with 40 μl of BRB12 buffer containing 20 μM taxol. Then,
767 40 μl of microtubule suspension in BRB12 buffer containing 20 μM taxol was infused and
768 incubated for 2 min. Then, 40 μl of BRB12 buffer containing 20 μM taxol and 1 mg/ml casein
769 was infused and incubated for 2 min. After washing with 40 μl of BRB12 buffer containing
770 20 μM taxol, the chamber was finally filled with observation buffer containing an ATP
771 regenerating system (10 μg/ml creatin kinase, 2 mM creatin phosphate), an oxygen
772 scavenging system (4.5 mg/ml glucose, 50 unit/ml glucose-oxidase, 50 unit/ml catalase, 0.5%
773 2-mercaptoethanol), 20 μM taxol, 200 nM Alexa Fluor 647 ATP (A22362; Invitrogen) and
774 100 pM kinesin in BRB12 buffer. All procedures were carried out at room temperature.
775
776 **Single molecule FRET observation**
777 Single molecule observation of fluorescently labeled kinesin was done under a prism-type
778 total internal reflection fluorescence microscopy (Mori et al., 2007). We used ATTO 488 (WT
779 monomer) and Cy3 (others) as a donor fluorophore. ATTO 488 was excited with 488 nm
780 diode laser (Cyan-75-TA-FE; Spectra-Physics Inc.) and Cy3 was excited with 515 nm diode
781 laser (EXLSR-515-50-CDTF-E, Spectra-Physics Inc.). Fluorescent signals were collected
782 through objective lens and a specific filter for cutting of the excitation light and projected on
783 a cooled EMCCD camera. For smFRET observations, fluorescent signal was separated using
784 dichroic mirror and donor and acceptor fluorescence were simultaneously observed. Position
785 of microtubule was identified based on the fluorescence from the labeled kinesin. When more
786 than 5 fluorescent spots of donor fluorophore lied on a straight line, we assumed that these
787 spots were on the microtubule. FRET data were collected at 10 ms and 200 ms exposure
788 times for wild-type monomer and for E236A monomer and E236A-WT heterodimer,
789 respectively, at 22 °C. We identified ATP binding to the kinesin head when the FRET
790 efficiency exceeded a threshold of 0.5.

791

792 **Gold labeling of kinesin**

793 Purified kinesin was biotinylated, and biotinylated kinesin was bound to microtubules in the
794 presence of AMP-PNP as described previously (Isojima et al., 2016). Microtubule-bound
795 kinesin was then collected by centrifugation (230,000*g* for 10 min) and was immersed in
796 streptavidin solution containing 12 mM PIPES (pH6.8), 2 mM $MgCl_2$, 1 mM EGTA, 20 μM
797 taxol and 2.5 mg/ml streptavidin (191-12851; Wako Pure Chemical Industries) and incubated
798 20 min at room temperature. Microtubule-bound streptavidin-modified kinesin was collected
799 by centrifugation (230,000g for 10 min) and released from microtubules as described
800 previously. Biotin-coated gold nanoparticles were prepared as previously described (Isojima
801 et al., 2016), except that streptavidin was not added to the gold. Just before observation,
802 streptavidin-modified kinesin and biotin-coated gold nanoparticles were mixed at a 1:1
803 molecule/particle ratio.

804

805 **Total internal reflection dark-field microscopy**

806 A flow cell was constructed, and microtubules were attached on the glass surface by using
807 protein A and anti-α-tubulin antibody as described previously (Isojima et al., 2016). The cell
808 was then infused with 40 μl of BRB 12 buffer (12 mM PIPES (pH 6.8), 2 mM EGTA and 1
809 mM $MgCl_2$) containing 20 μM taxol and 1 mg/ml casein for 2 min. The cell was infused with
810 BRB12 buffer containing 3 nM gold-labeled kinesin for 5 min, and unbound kinesins and
811 gold nanoparticles were removed by washing with 60 μl of the BRB12 buffer containing 20
812 μM taxol. Finally, the flow cell was infused with 40 μl of the observation buffer (BRB12
813 buffer containing 70 mM β-mercaptoethanol, 10 μg/ml creatine kinase, 2 mM creatine
814 phosphate, 20 mM KCl and 1-1000 μM ATP), sealed with nail polish and used for observation.
815 All procedures were carried out at room temperature. The gold-labeled kinesin was observed
816 using a total internal reflection dark-field microscope as described previously (Isojima et al.,
817 2016) and the scattering images were recorded with a high-speed CMOS camera (FASTCAM
818 Mini AX100; Photron) at a frame rate of 20,000 fps (50 μs temporal resolution). Observations
819 were carried out at 24-26°C.

820

821 **Data analysis for the dark-field observations**

822 The coordinates of gold nanoparticles were determined as described previously (Isojima et
823 al., 2016). The orientations of the microtubule 'on axis' (orientation parallel to the
824 microtubule long axis) and 'off axis' (orientation perpendicular to the microtubule long axis)
825 were then determined from the aligned gold-labeled kinesin along the microtubule and
826 adjusted to X and Y coordinates as described previously. The 'bound' and 'unbound' states
827 of gold-labeled kinesin heads were determined as follows: two-dimensional standard
828 deviation (s.d.) of the trajectory for each time frame t was calculated as [t - 20, t + 20] and
829 the median μ and s.d. σ of the s.d. of the trajectory was determined by fitting the histogram
830 of the s.d. with a Gaussian function. Transitions from the bound to unbound state were
831 detected when the s.d. was higher than μ+4σ in 10 consecutive frames and transition from
832 the unbound to bound state were detected when the s.d. was lower than μ+4σ in 10
833 consecutive frames. The accurate frame of the transition was determined by fitting the on-
834 and off-axis trajectory near the transition with two state step function. In the case of G0
835 construct, if two unbound states were closer than 50 ms and on-axis average of the bound
836 state between these unbound states was separated from the other bound states, these unbound
837 states and bound state were determined as unbound state 1-3 (**Figure 4–figure supplement**
838 **2**). The rate constants of each state were determined by fitting the histogram of the dwell time
839 with single exponential functions.

840

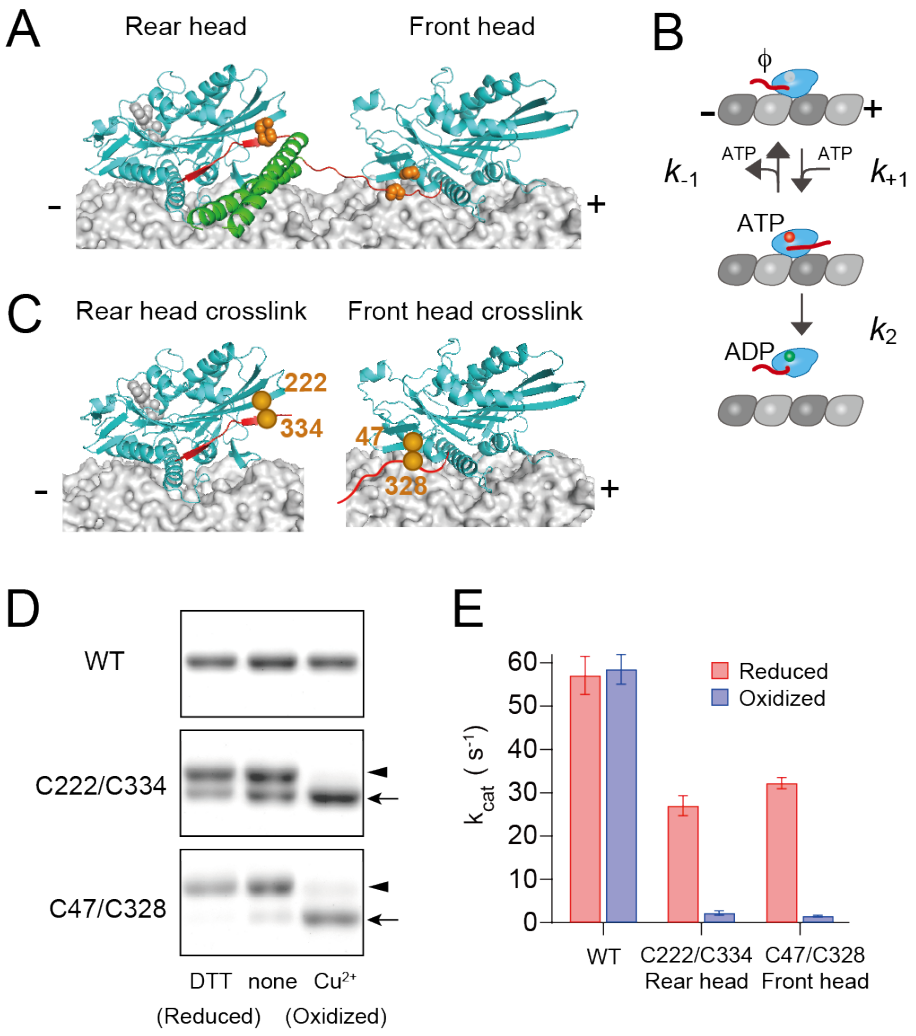

Figure 1. Disulfide-crosslinking to constraint the neck linker in either the forward or backward pointing configuration. (**A**) Three-dimensional structure of kinesin dimer on the microtubule in the two-head-bound intermediate state (modeled based on PDB# 4HNA and 4LNU). The motor domain, neck linker, and neck coiled-coil are shown in cyan, red, and green. Orange spheres represent the positions of cysteine residues as described in panel **C**. (**B**) Michaelis-Menten kinetics scheme for ATP-promoted dissociation of kinesin head from the microtubule, which includes ATP-binding (k_{+1}), ATP-dissociation (k_{-1}), and ATP-induced microtubule-dissociation (k_2) steps. (**C**) Positions of the cysteine residues for disulfide-crosslinking of monomeric kinesin. Cys222 and Cys334 were introduced to constrain the neck linker in the forward, docked conformation (left), while Cys47 and Cys328 were introduced to constrain the neck linker in the backward-pointing configuration (right). (**D**) Disulfide crosslinking after oxidative treatment was analyzed by nonreducing SDS-PAGE. WT (without Cys introduction), C222/C334, and C47/C328 constructs were treated with a reducing reagent (DTT), none, or oxidizing reagents (Cu^{2+}). Arrows and arrowheads indicate

un-crosslinked and intramolecular crosslinked kinesins, respectively. The whole image of the gels is shown in **Figure 1–figure supplement 1**. (**E**) Microtubule-activated ATPase under reduced and oxidized conditions. k_{cat} and K_m(MT) were determined from the fit to a Michaelis-Menten equation of ATP turnover rates at various microtubule concentrations (**Figure 1–figure supplement 2**). Mean ± s.e.m. values were obtained from three independent assays.

Figure supplement 1. Estimation of disulfide-crosslinking efficiency.

Figure supplement 2. Steady-state microtubule-activated ATPase rates of monomeric kinesins before and after oxidative crosslinking.

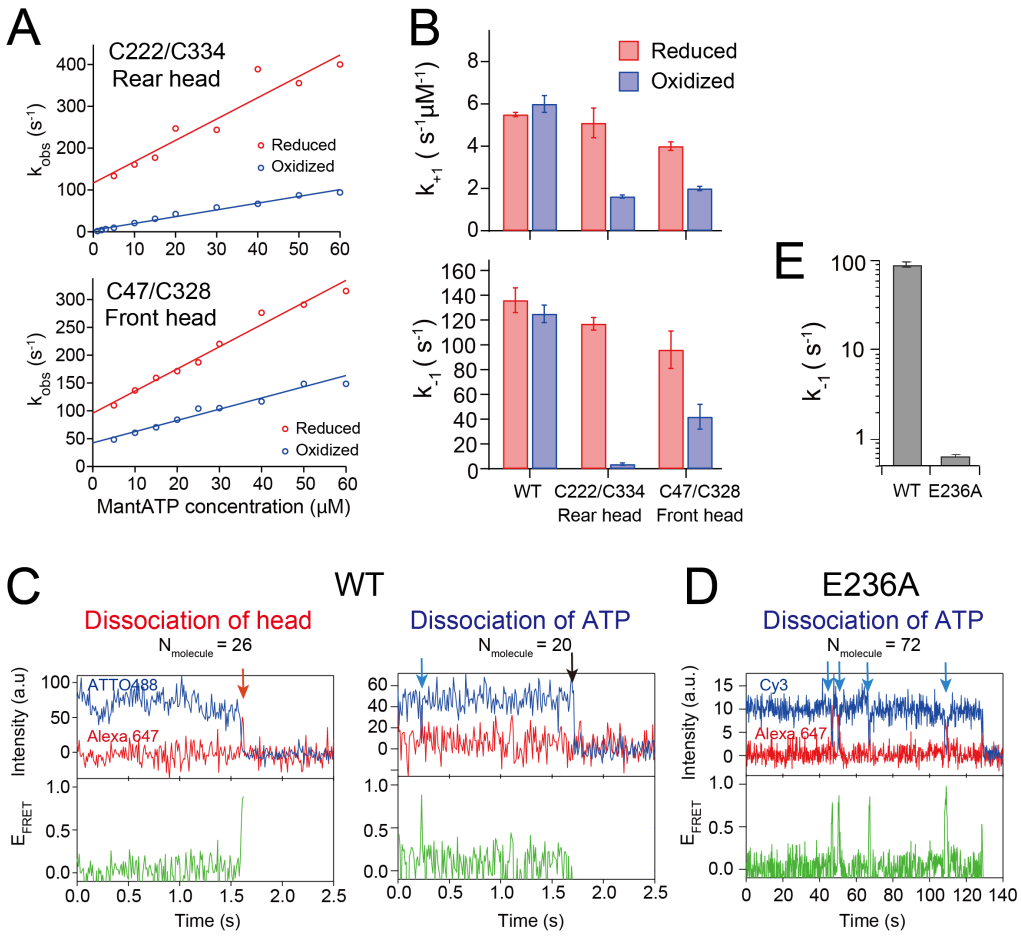

Figure 2. ATP-binding/dissociation kinetics of disulfide-crosslinked monomers. (**A**) The rate of initial enhancement of the fluorescence after rapid mixing of kinesin-microtubule complex with mant-ATP (k_{obs}; **Figure 2–figure supplement 1**) was plotted as a function of mant-ATP concentration. Solid lines represent a linear fit; the slope provides the on-rate of mant-ATP (k_{+1}) and the off-set provides the off-rate of mant-ATP (k_{-1}). (**B**) ATP binding rate k_{+1} and ATP dissociation rate k_{-1} of monomers before and after crosslinking obtained from the fit shown in pane **A**. Error bar shows the fit error. (**C**) Two typical traces of smFRET between the donor-labeled wild-type monomer and Alexa-ATP (500 nM). Fluorescence intensities of donor (blue) and acceptor (red), and the calculated FRET efficiency (green) recorded at 100 fps are shown. Left trace: the FRET efficiency transiently increases just before both dyes disappear (indicated by the red arrow), suggesting that the nucleotide-bound head detached from the microtubule (**Figure 2–figure supplement 3A**). Right trace: the FRET efficiency transiently increases, followed by the recovery of donor fluorescent (shown by the blue arrow), indicating the reversible dissociation of ATP. The black arrow indicates the photobleaching of the donor dye. The numbers of molecules observed for each type is shown at the top of the traces. (**D**) Typical trace of smFRET between the E236A monomer and Alexa-ATP (200 nM) recorded at 5 fps, demonstrating repetitive ATP binding and dissociation. (**E**) The dissociation rate k_{-1} of Alexa-ATP from wild-type and E236A

monomers (histograms are shown in **Figure 2−figure supplement 3B**). The value for the wild-type may be underestimated due to the limited temporal resolution (10 ms).

Figure supplement 1. Pre-steady-state kinetics of ATP binding to monomeric kinesin-microtubule complex before and after crosslinking.

Figure supplement 2. Processive motility of wild-type kinesin dimer driven by Alexa 647 ATP.

Figure supplement 3. Dwell time of Alexa-ATP-bound state for wild-type and E236A monomers determined using smFRET.

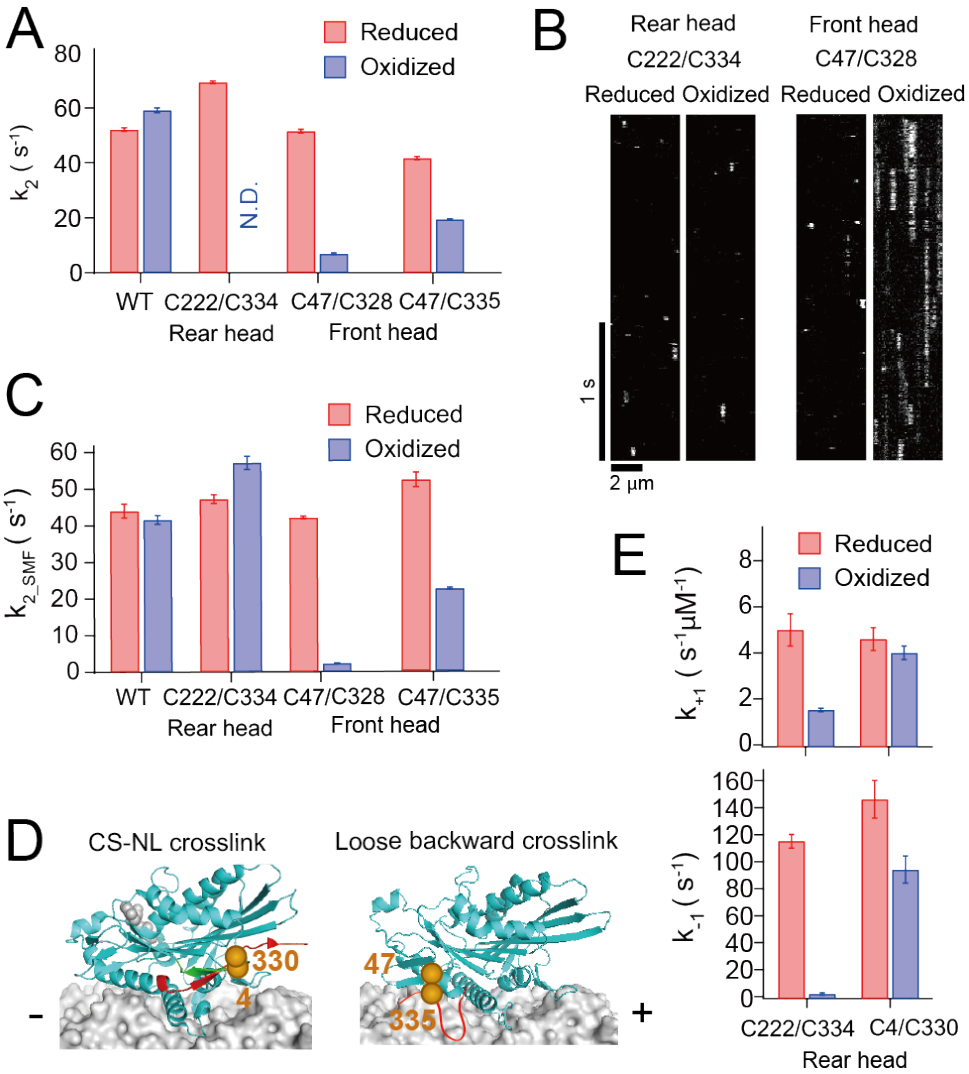

Figure 3. Microtubule-detachment kinetics of disulfide-crosslinked monomers. (**A**) ATP-induced dissociation rate from microtubule k_2 measured by turbidity change after the rapid mixing of kinesin-microtubule complex with 1 mM ATP. The turbidity time traces are shown in **Figure 3–figure supplement 1**. (**B**) Kymographs showing the binding and dissociation of GFP-fused kinesin under reduced and oxidized conditions on the microtubule. C47/C328 showed an extended dwell on the microtubule after crosslinking. (**C**) ATP-induced dissociation rate from the microtubule measured using single-molecule observations of GFP-fused kinesin. k_{2_SMF} was determined as an inverse of the mean dwell time of the fluorescent kinesin on the microtubule in the presence of 1 mM ATP. The dwell time histograms are shown in **Figure 3–figure supplement 2B**. (**D**) Positions of Cys4 and Cys330 residues for disulfide-crosslinking of a monomer between the N-terminal cover strand (CS; green) and the neck linker (NL; red) (left). Positions of Cys47 and Cys335 residues for disulfide-crosslinking of a monomer to constrain the neck linker in the backward-pointing configuration allowing partial docking of the neck linker (right; **Figure**

3−figure supplement 3). The ATP-induced dissociation rates from the microtubule of C47/C335 monomer before and after crosslinking, measured by turbidity change (k_2) and single-molecule fluorescence (k_{2_SMF}), are shown in **Figure 3A, C**. Histograms are displayed in **Figure 3−figure supplement 4E**. (**E**) Mant-ATP binding rate k_{+1} and dissociation rate k_{-1} of C4/C330 monomer before and after crosslinking (data for C222/C334 are included from **Figure 2B** for comparison). The k_{obs} plots are shown in **Figure 3−figure supplement 4B**.

Figure supplement 1. ATP-induced dissociation kinetics of crosslinked kinesin from microtubule measured using light scattering.

Figure supplement 2. ATP-dependent microtubule-binding and -dissociation of crosslinked kinesins observed by single-molecule fluorescence microscopy.

Figure supplement 3. Locations of the C47/C328 and C47/C335 residues when the labeled head is in the front or rear of dimeric kinesin.

Figure supplement 4. Kinetics measurements of ATP-binding and microtubule-dissociation of C4/C330 and C47/C335 crosslinked monomeric kinesins.

			Rear head		Front head	
	WT		C222/C334		C47/C328	
	Reduced	Oxidized	Reduced	Oxidized	Reduced	Oxidized
k_{cat} (s^{-1})	57.1 ± 4.4	58.5 ± 3.4	27.0 ± 2.3	2.2 ± 0.5	32.2 ± 1.3	1.5 ± 0.2
K_m(MT) (μM)	0.31 ± 0.08	0.36 ± 0.08	0.23 ± 0.06	0.200 ± 0.007	0.28 ± 0.06	0.13 ± 0.04
k_{+1} ($s^{-1}\mu M^{-1}$)	5.5 ± 0.1	6.0 ± 0.4	5.1 ± 0.7	1.62 ± 0.07	4.0 ± 0.2	2.0 ± 0.1
k_{-1} (s^{-1})	136 ± 5	125 ± 12	117 ± 23	3.7 ± 1.9	96 ± 6	42 ± 4
k_2 (s^{-1})	52.1 ± 0.6	59.1 ± 0.9	69.3 ± 0.5	N.D.	51.5 ± 0.7	7.0 ± 0.3
k_{2_SMF} (s^{-1})	44.0 ± 1.9	41.6 ± 1.2	47.2 ± 1.2	57.1 ± 2.3	42.1 ± 0.4	2.30 ± 0.08

	C4/C330		C47/C335	
	Reduced	Oxidized	Reduced	Oxidized
k_{cat} (s^{-1})	33.5 ± 2.1	32.6 ± 1.2	43.1 ± 3.0	11.9 ± 0.6
K_m(MT) (μM)	0.42 ± 0.08	8.36 ± 0.98	0.33 ± 0.05	0.10 ± 0.01
k_{+1} ($s^{-1}\mu M^{-1}$)	4.7 ± 0.5	4.1 ± 0.3	9.1 ± 0.3	4.5 ± 0.1
k_{-1} (s^{-1})	148 ± 18	96 ± 9	85 ± 10	41 ± 5
k_2 (s^{-1})	68.6 ± 0.5	80.8 ± 0.8	41.6 ± 0.6	19.4 ± 0.2
k_{2_SMF} (s^{-1})	59.5 ± 2.3	58.4 ± 2.6	52.1 ± 2.0	22.5 ± 0.3

Table 1. Kinetic rate constants for disulfide-crosslinking monomers. Steady-state ATP-turnover rate (k_{cat} and K_m(MT)), pre-steady-state mant-ATP binding (k_{+1} and k_{-1}) and microtubule dissociation rates (k_2 and k_{2_SMF}, measured by light scattering and single-molecule fluorescence) measured under reduced and oxidized conditions.

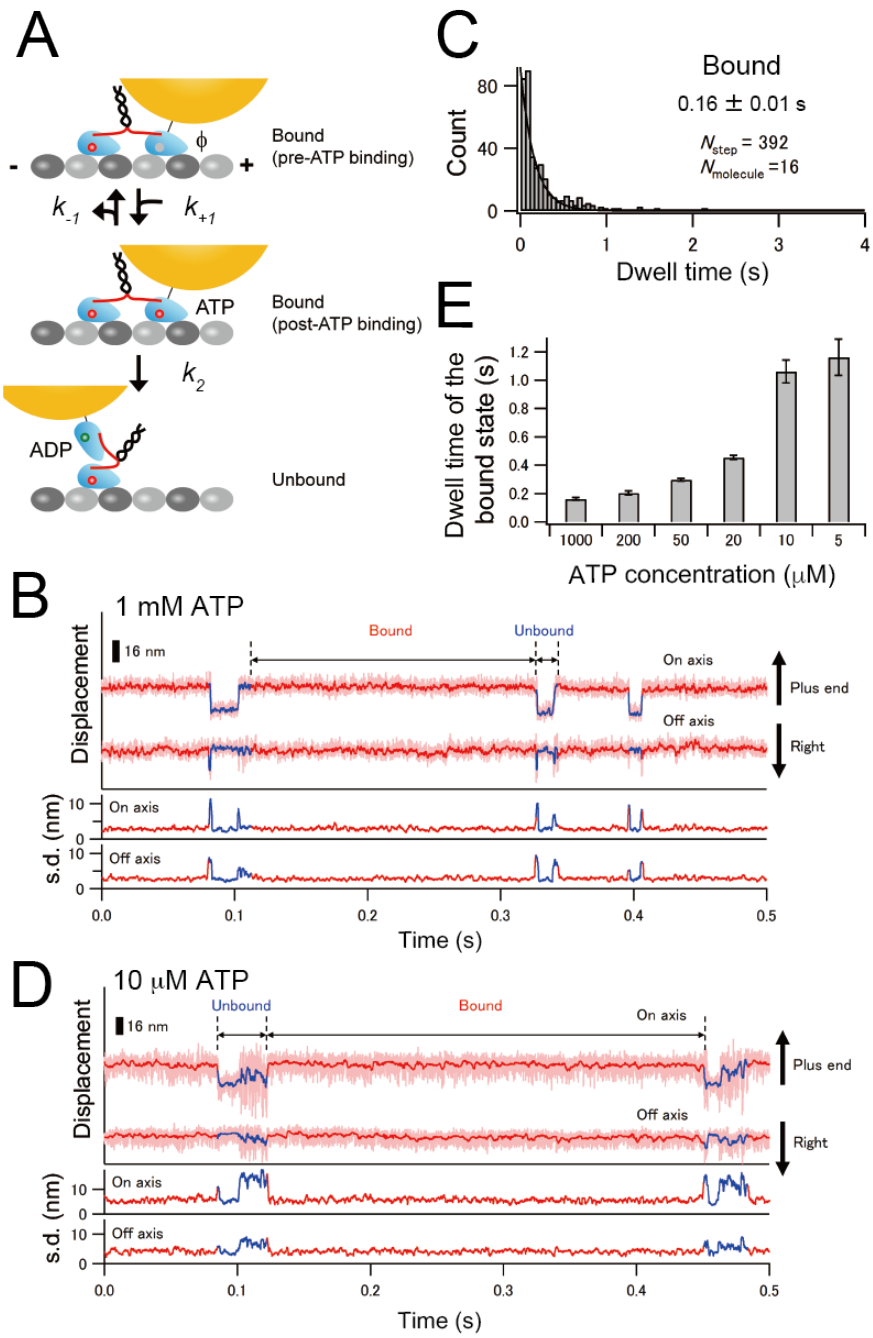

Figure 4. Microtubule-detachment kinetics of the front WT head of E236A-WT heterodimer. (**A**) A diagram illustrating the kinetic transitions for the detachment of the gold-labeled WT head of the E236A-WT heterodimer. Upon binding to the microtubule, the front head releases ADP, becoming a nucleotide-free state (indicated as ϕ; pre-ATP binding). The detachment kinetics from this state can be described using the same scheme as the monomer (**Figure 1B**). (**B**) Typical trace for the centroid positions of the gold probe attached to the WT head of the E236A-WT heterodimer in the presence of 1 mM ATP (light red lines), toward the microtubule long axis (on axis) and perpendicular to the microtubule

axis (off axis). Red and blue lines depict the median-filtered trace (with a window size of 51 frames) for the bound and unbound states, respectively. Lower panels display the standard deviation (s.d.) of on- and off-axis positions for each time frame t (calculated as [t – 20, t + 20]). (**C**) Histogram of the dwell time in the bound state. The solid line shows the fit with an exponential function. The number represents the average dwell time (± s.e.m.) determined from the fit. (**D**) Typical trace for the centroid positions of the gold probe attached to the WT head of E236A-WT heterodimer in the presence of 10 μM ATP. (**E**) Mean dwell times in the bound state under various ATP concentrations as determined from the fit of the histograms of the dwell times (**Figure 4-figure supplement 5**).

Figure supplement 1. Single-molecule FRET between two heads of E236A-WT heterodimer.

Figure supplement 2. The unbound state of the gold-labeled WT head of the E236A-WT heterodimer.

Figure supplement 3. Long-term trace of the gold-labeled E236A-WT heterodimer exhibiting very slow stepping motion.

Figure supplement 4. Distributions of the dwell time in the bound and unbound states of the leading WT head of E236A-WT heterodimer.

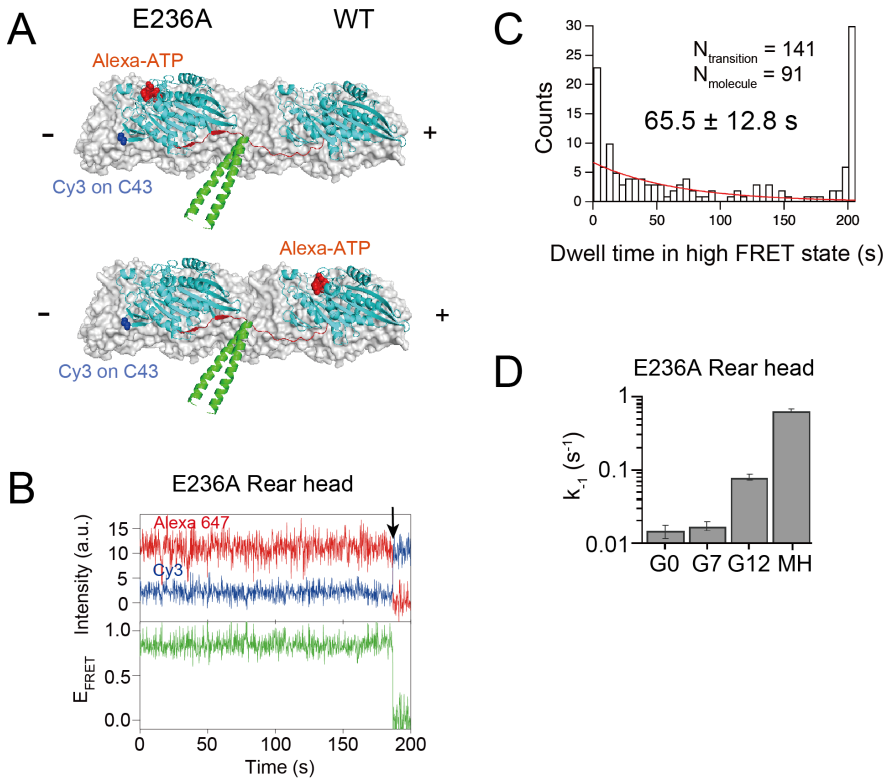

Figure 5. ATP-dissociation kinetics of the rear head of E236A-WT heterodimer (**A**) Diagram showing the position of Cys43 residue of E236A chain for labeling with donor (Cy3; blue) fluorophore, and the Alexa 647 ATP (red) bound to the rear E236A head (upper) or the front wild-type head (lower) of the E236A-WT heterodimer. High FRET efficiency is expected when the Alexa-ATP binds specifically to the rear E236A head. (**B**) Typical trace of fluorescence intensities of donor (Cy3; blue) on the E236A rear head and acceptor (Alexa 647; red) fluorophores, calculated FRET efficiency (green), for E236A-WT heterodimer in the presence of 200 nM Alexa-ATP recorded at 5 fps. The black arrow indicates the dissociation of Alexa-ATP, accompanied by the recovery of donor fluorescent. ATP remains bound to the rear head for a significantly longer duration compared to the monomer (**Figure 2D**). (**C**) Histogram of the dwell time of the high FRET state. The red lines show fit with an exponential decay. The number represents the average dwell times (± s.e.m.) determined from the fit. The inverse of the mean dwell time k_{-1} is 0.015 ± 0.003 s^{-1}. (**D**) The ATP dissociation rates k_{-1} for the E236A rear head of the wild-type (G0), G7 and G12 E236A-WT heterodimer were determined using smFRET. The k_{-1} was calculated as the inverse of the mean dwell time for the high FRET state (see the typical trace and dwell time histograms for the G7 and G12 heterodimer in **Figure 5-figure supplement 1**). For comparison, data for the E236A monomer head (referred to as MH) is included from **Figure 2E**.

Figure supplement 1. Single molecule FRET between donor-labeled E236A head of E236A-WT heterodimer with extended neck linker and acceptor-conjugated ATP.

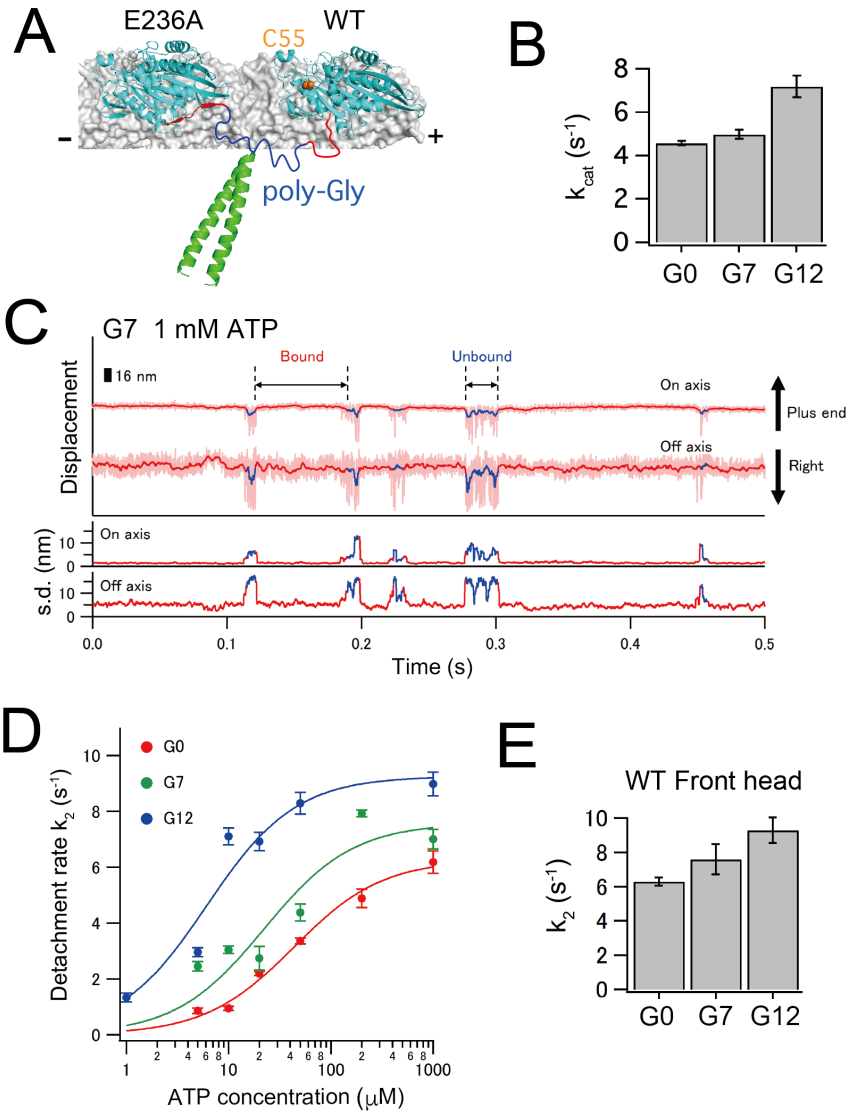

Figure 6. Effect of the tension applied to the neck linker on the gating examined using the neck-linker extended E236A-WT heterodimer. (**A**) Diagram showing the position of the poly-Gly residues (blue) inserted between the neck linker (red) and the neck coiled-coil (green). The Cys55 residue for gold-labeling is represented by an orange sphere. (**B**) k_{cat} for the microtubule-activated ATPase of E236A-WT heterodimers without (termed as G0) and with neck-linker extensions (G7 and G12) (**Figure 6-figure supplement 1**). (**C**) Typical trace for the centroid positions of the gold probe attached to the WT head of the E236A-WT heterodimer with a 7 poly-Gly insertion in the presence of 1 mM ATP. (**D**) The inverse of the mean dwell time in the bound state was plotted as a function of ATP concentration, as determined from the fit of the histograms of the dwell times (**Figure 6-figure supplement 2, 3**). Error bars represent s.e.m. The solid lines show the fit with the Michaelis-Menten equation. The fit parameters are k_{cat} (or k_2) = 6.3 ± 0.2 s^{-1} and K_m (ATP) = 43 ± 6 μM for G0, k_{cat} = 7.0 ± 0.5 s^{-1} and K_m (ATP) = 12 ± 3 μM for G7, and k_{cat} = 9.3 ± 0.7 s^{-1} and K_m (ATP) = 6.1 ± 2.1 μM for G12. The K_m (ATP) decreases as the insertion length increases.

(**E**) The k_{cat} value, which represents the ATP-induced detachment rate of the front head k_2, obtained from the fit shown in panel **d**. The error bars represent s.e.m.

Figure supplement 1. Microtubule-activated ATPase rates of the E236A-WT heterodimer with and without neck-linker extension.

Figure supplement 2. Distributions of the dwell time in the bound and unbound states of the leading WT head of E236A-WT heterodimer with 7 poly-Gly insertion (G7).

Figure supplement 3. Distributions of the dwell time in the bound and unbound states of the leading WT head of E236A-WT heterodimer with 12 poly-Gly insertion (G12).

Figure supplement 4. Binding to the rear-tubulin binding site observed for the G12 E236-WT heterodimer.

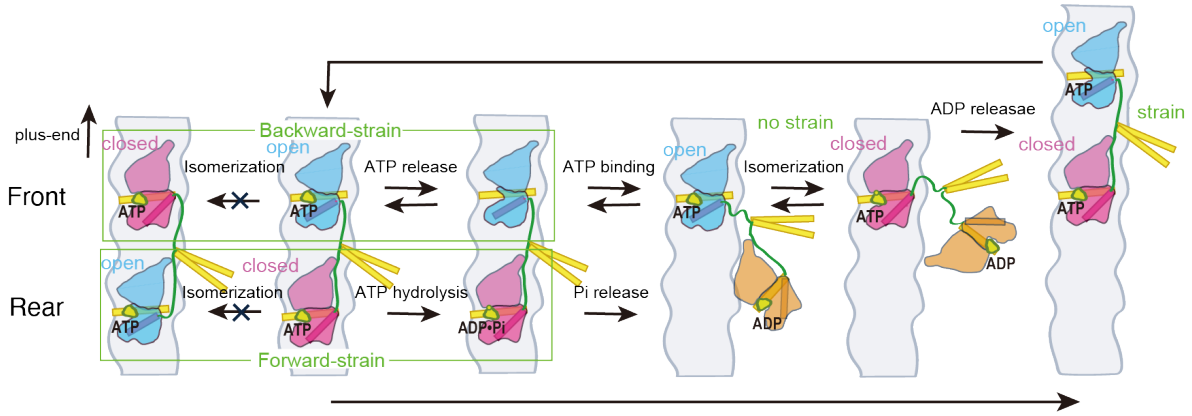

Figure 7. Model to explain how the tension exerted by the stretched neck linker in dimeric kinesin coordinates the microtubule detachment of the two heads. This model is based on the proposal that the transition between ATP-bound open and closed conformations of the head is regulated by the neck linker strain (**Figure 7-figure supplement 2**). The open and closed conformational states of the head are indicated in blue and red, respectively, with the α6 helix, which connects to the neck linker, highlighted as a rod. The microtubule-detached ADP-bound state is shown in orange. The neck linker is depicted in green, while the α4 helix, which directly interacts with the microtubule, and the neck coiled-coil are shown in yellow. In the two-head-bound state, the front head remains in the open state because the backward strain prevents it from transitioning to the closed state. In this state, ATP can weakly bind to the nucleotide-pocket but often dissociates. Conversely, the rear head is stabilized in the closed state because the transition to the open state is suppressed by the forward strain. ATP is tightly bound to the closed nucleotide-pocket, causing the rear head to hydrolyze ATP and detach from the microtubule before the front head does. In the one-head-bound state, the microtubule-bound head can transition between the open and closed states. However, once the tethered head binds preferentially to the forward tubulin-binding site, the strain built up between the two microtubule-bound heads stabilizes the rear head in the closed conformation and the front head in the open conformation.

Figure supplement 1. Structural difference between the open and closed conformational states of the kinesin head.

Figure supplement 2. Schematic model showing that the open-closed conformational transition (isomerization) is gated by the neck linker strain.